International Journal of Multiphase Flow 104 (2018) 166–173

Contents lists available at ScienceDirect

International Journal of Multiphase Flow

journal homepage: www.elsevier.com/locate/ijmulflow

A comparative analysis of the effective and local slip lengths for liquid flows over a trapped nanobubble

Haibao Hu[a,b,*], Dezheng Wang[a], Feng Ren[a], Luyao Bao[a], Nikolai V. Priezjev[c,*], Jun Wen[a]

[a] School of Marine Science and Technology, Northwestern Polytechnical University, Xi'an, Shanxi 710072, People's Republic of China
[b] Research & Development Institute in Shenzhen, Northwestern Polytechnical University, Shenzhen 518057, People's Republic of China
[c] Department of Mechanical and Materials Engineering, Wright State University, Dayton, OH 45435, USA

ARTICLE INFO

Article history:
Received 21 November 2017
Revised 28 February 2018
Accepted 3 March 2018
Available online 7 March 2018

Keywords:
Hydrophobic
Drag reduction
Wettability difference
Gas layer
Slip

ABSTRACT

The gas–liquid interfaces distributed on a superhydrophobic (SHP) surface promote the effective slip and might result in significant drag reduction desirable in many applications. While the slippage of water past gas–liquid interfaces on structured SHP surfaces has attracted wide attention, the slip behavior at gas–liquid interfaces trapped by the wettability step still remains unclear. Using molecular dynamics simulations, we first demonstrated that the three-phase contact line can be pinned on a smooth substrate of mixed wettability. We then numerically investigated slip flows over smooth surfaces with flattened gas bubbles trapped by the wettability step. It was found that the local slip length is relatively large at the gas–liquid interface and its spatial distribution becomes asymmetric due to shear-induced deformation of the attached bubble, while the effective slip length remains nearly constant. With increasing gas areal fraction, the local and effective slip lengths become larger, especially in the case of a stripe-like continuous gas–liquid interface where the interface curvature in the flow direction is absent.

1. Introduction

Bioinspired superhydrophobic surfaces are important for many technological applications that involve drag reduction, self-cleaning and nonfouling surfaces as well as heat transfer (Bidkar et al., 2014; Lee and Kim, 2009; Ou et al., 2004; Ou and Rothstein, 2005; Rothstein, 2010). The chemical and topographical features of these special surfaces allow the formation of locally stable air-water interfaces that reduce the skin frictional drag by violating the assumption of no-slip boundary condition (Hemeda and Tafreshi, 2016; Lee et al., 2008; Nizkaya et al., 2016; van Limbeek and Seddon, 2011; Yang et al., 2007). The so-called slip length, which is often used to describe flows near interfaces of gas–liquid or liquid–liquid (Razavi et al., 2014), was originally introduced by Navier and it is commonly used to quantify the degree of slip. Geometrically, the slip length L_s is defined as an extrapolated distance with respect to the interface where the fluid velocity profile vanishes (Yen, 2015; Thalakkottor and Mohseni, 2016). For small scale flows the slip effect can be significant. For example, in a circular pipe with diameter D, the slip length L_s results in an increase of the flux by a factor of $1 + 8L_s/D$ (Lauga and Stone, 2003).

Over the past decades, a number of studies have been carried out to investigate the effective slip flows in the presence of gas–liquid interfaces at superhydrophobic surfaces (Hyvaluoma et al., 2011; Lee and Kim, 2009; Teo and Khoo, 2014). It is well established that the magnitude of the effective slip length, that describes flow far away from the surface, depends on the geometric characteristics of a gas–liquid interface, the topography of a solid substrate, and the gas areal fraction, φ_g, which is the fraction of a surface covered by the gas phase. Choi et al. studied a liquid flowing over a solid surface covered with a uniform gas layer, and found that the slip length of 50 μm is expected if the gas layer is 1-μm-thick air in water at room temperature (Choi et al., 2006). On the other hand, if the depinned contact line spreads on the top of surface structures, for example, due to liquid shear flow, as shown in the numerical study of Feng and Basaran (1994), the overgrown gas pockets may enhance slip. In laminar flows, it has been shown that the shape of the air–water interface is an important factor in drag reduction. Using scaling arguments, Ybert et al. proposed that the effective slip length increases with the gas areal fraction as $\sim 1/(1-\varphi_g)$ for a flat gas–liquid interface (Ybert et al., 2007). In the presence of a meniscus, the effective slip is reduced due to curvature of the flow (Teo and Khoo, 2014). Karatay et al. produced microbubbles at the boundary of the superhydrophobic microchannel using microfluidic devices. The slip length was found to decease with increasing bubble protrusion angles. In addition, the

* Corresponding authors.
E-mail addresses: huhaibao@nwpu.edu.cn (H. Hu), nikolai.priezjev@wright.edu (N.V. Priezjev).

https://doi.org/10.1016/j.ijmultiphaseflow.2018.03.001
0301-9322/

topography of a solid substrate might also influence the effective slip length (Karatay et al., 2013). Using scaling analysis and continuum simulations, Cottin-Bizonne et al. demonstrated that the effective slip length at interfaces that consist of single-scale post structures is always larger than in the cases of hierarchical fractal structures with the same gas areal fraction (Cottin-Bizonne et al., 2012). Vinogradova et al. studied how the wettability and roughness of a solid impact its hydrodynamic properties and found that hydrophobic slippage can be dramatically affected by the presence of surface roughness (Vinogradova and Belyaev, 2011; Priezjev and Troian, 2006). In general, the relative slipping near the moving contact line is proportional to the sum of tangential viscous stress and the uncompensated Young stress (Qian et al., 2003; Thalakkottor et al, 2016). Other factors such as surface impurities will also influence the slip behavior; for example, Maali et al. found that very low concentrations of surface impurities drastically modify boundary conditions for interfacial flows (Maali et al., 2017).

In the analysis of boundary slip, the assumption of perfectly slipping liquid over islands of trapped gas phase is commonly used. However, among others, recent experiments by Bolognesi et al. (2014) using a micro Particle Image Velocimetry (micro-PIV), have demonstrated that the shear stress is, in general, non-zero at the gas–liquid interface. More recently, Schaffel et al. reported a detailed investigation of the flow field and local slip length of water over a microstructured superhydrophobic surface. Surprisingly, their results have shown that the local slip length at the air-water interface is anisotropic and it depends strongly on the surface topography (Schaffel et al., 2016). Despite significant progress, it is still unclear to what extent the gas–liquid interface affects the effective slippage, since the correlation between the slip length and geometric characteristics of a gas–liquid interface may be significantly influenced by the edges of surface irregularities.

The objective of the present study is to investigate the effect of the gas–liquid interface on the local and effective slip lengths using molecular dynamics simulations. In order to exclude the effect of surface roughness, the wettability step is introduced on a smooth solid substrate that pins the three-phase contact line of the gas–liquid interface. After demonstrating that the gas phase can be effectively trapped by the surface wettability step (see MD simulations in Section 2 and experiments in supplementary information section), we perform a comparative analysis of the position-dependent effective and local slip lengths at the gas–liquid interface. Interestingly, the local slip length at the composite interface is found to be anisotropic even in the absence of surface roughness, while the effective slip length remains nearly constant. Finally, the relationship between the slip lengths and gas areal fraction is examined in detail for different flow conditions. The simulation results indicate that drag is reduced for gas–liquid interfaces when the interface curvature in the flow direction is absent.

2. MD simulation method

The MD setup consists of a liquid slab confined between two atomically smooth solid walls as illustrated schematically in Fig. 1. The dimensions of the fluid domain are measured $L_x \times L_y \times L_z = 200$ Å $\times$ 100 Å $\times$ 100 Å (without solid walls). The interaction between any two atoms is modeled by the truncated Lennard–Jones (LJ) potential:

$$E_{ij} = \begin{cases} 4\varepsilon_{\alpha\beta}\left[\left(\frac{\sigma_{\alpha\beta}}{r_{ij}}\right)^{12} - \left(\frac{\sigma_{\alpha\beta}}{r_{ij}}\right)^{6}\right], & r < r_c \\ 0, & r \geq r_c \end{cases} \quad (1)$$

where E_{ij} is energy between atoms i and j that belong to either liquid, solid or gas phases. In Eq. (1), the parameters ε, σ and r_c are the characteristic energy, length and the cutoff distance ($r_c = 8.5125$) Å of the LJ potential. The indices $\alpha\beta$ denote types

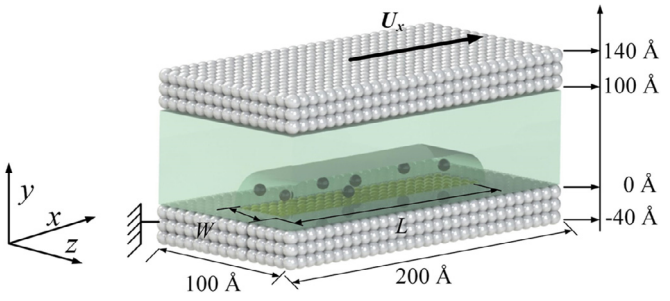

Fig. 1. Illustration of the simulation domain. The symbols (•), (•), (•) and (■) denote the wetting solid, non-wetting solid, gas atoms and liquid phase, respectively. The liquid consists of 13,750 atoms, each wall contains 15,225 atoms, and the gas phase is formed by 78 atoms. The reference plane at $y = 0$, the channel height, and the wall thickness are indicated on the vertical axis (y).

of atoms i and j, and refer to either solid–solid (ss), liquid–liquid (ll), gas–gas (gg), liquid–gas (lg), solid–gas (sg) or solid–liquid (sl). In our study, the rigid wall model was adopted where wall atoms are fixed to the sites of the face-centered-cubic (fcc) lattice (see Fig. 1).

The parameters of the LJ potential $\varepsilon_{\alpha\alpha}$ for l, s and g are 0.043, 0 and 0.01042 eV, respectively, and the corresponding values of $\sigma_{\alpha\alpha}$ are set to 3.405, 0 and 3.405 Å. In turn, the values of ε_{sg} and ε_{lg} are 0.0001 and 0.001 eV, and the corresponding values of σ_{sg} and σ_{lg} are both equal to 3.405 Å. The length scale of the LJ potential between solid atoms and liquid monomers is set $\sigma_{sl} = 3.154$ Å throughout the study. The fcc lattice constant of the solid walls is fixed to 3.186 Å. The liquid phase consists of 13,750 atoms, each wall contains 15,225 atoms, and the gas phase contains 78 atoms. Finally, the densities of the solid, liquid and gas phases are $\rho_s = 0.1254$ Å^{-3}, $\rho_l = 0.0207$ Å^{-3}and $\rho_g = 0.00257$ Å^{-3}after thermal equilibrium in static state, respectively.

To characterize surface wetting properties, the interaction energy between the solid and liquid phases was determined using the relation $\theta = cos^{-1}(2\frac{\varepsilon_{sl}}{\varepsilon} - 1)$, where $\varepsilon = 0.043eV$ and θ is the contact angle. The wettability step was created by spatially adjusting the interaction energy between the liquid monomers and atoms of the lower solid wall. More specifically, the non-wetting region of the lower wall with the surface energy $\varepsilon_{sl} = 0.0001eV$ was surrounded by the wetting area with the surface energy $\varepsilon_{sl} = 0.043eV$ (see Fig. 1). The corresponding values of the contact angle for spatially uniform surfaces with surface energies $\varepsilon_{sl} = 0.0001eV$ and $\varepsilon_{sl} = 0.043eV$ are 160°and 0°, respectively. The length and width of the non-wetting region are denoted by L and W, respectively, as shown in Fig. 1. Our simulation results demonstrate that a nanobubble can be attached at the smooth surface of mixed wettability and it remains stable even in a shear flow. The pinning mechanism of the three-phase contact line by the wettability step will be discussed separately in Section 3.1.

The Couette shear flow was induced in the fluid domain by translating the upper wall with a constant velocity U_x along the x direction, while the lower wall was kept stationary. Periodic boundary conditions are applied along the flow direction x and the neutral direction z.

All simulations were carried out using the LAMMPS open-source MD package (Plimpton, 1995). The system temperature is maintained at $T = 300K$ by the Nosé–Hoover thermostat (Yong and Zhang, 2013a). The equations of motion are integrated using the velocity-Verlet algorithm with the time step $\Delta t = 0.002$ ps. The computational domain is divided into small cubes with the size of 3 Å $\times$ 3 Å $\times$ 3 Å that were used for averaging the density and velocity fields. After the equilibration period of about 10^5 MD time steps, a typical run required at least 10^6 MD time steps to reach a

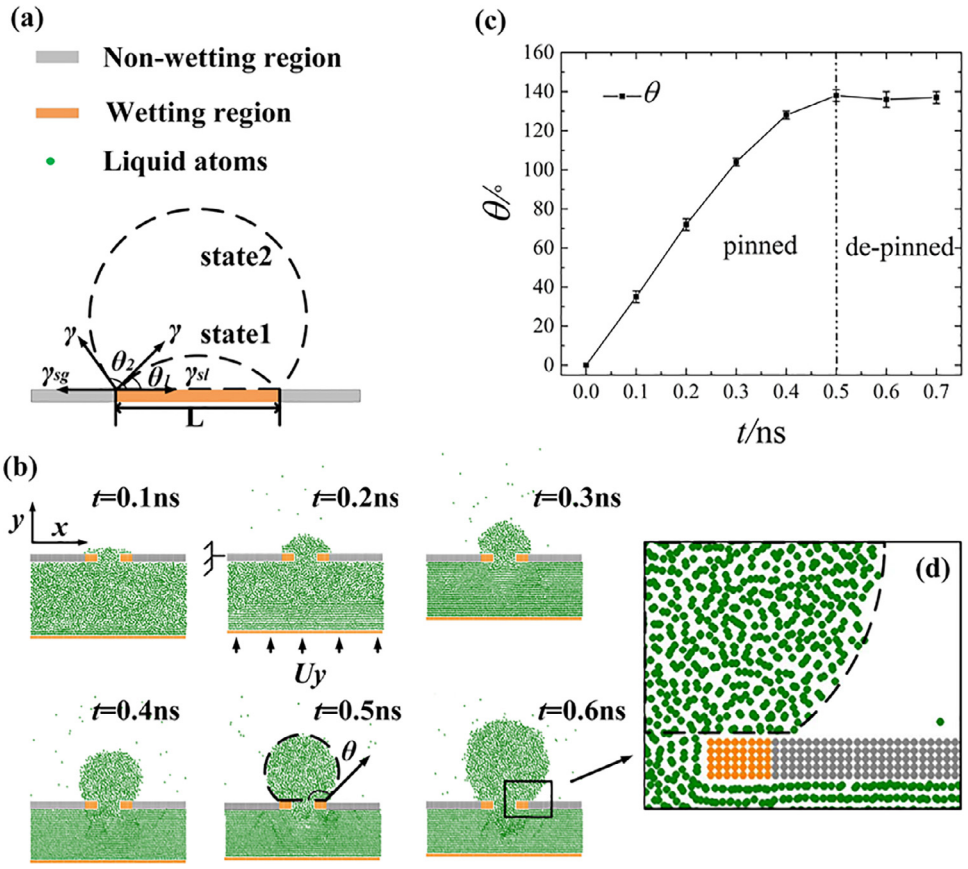

Fig. 2. The pinning mechanism of the three-phase contact line by the wettability step. (a) A schematic diagram of the liquid droplet on the surface of mixed wettability. (b) A sequence of snapshots of the liquid droplet pinned at the edges of the wetting region (the wetting region with ε_{sl}= 0.043*eV*, the non-wetting region with ε_{sl}= 0.0005*eV*). (c) The variation of the contact angle as a function of time. (d) An enlarged view of the liquid droplet with de-pinned contact line.

steady Couette flow. The measured quantities of interest were averaged during an additional time interval of 2×10^7 MD steps.

3. Results and discussions

3.1. The pinning mechanism of the three-phase contact line

The pinning of the three-phase contact line on a smooth substrate by patterned hydrophobic/hydrophilic stripe is novel. Therefore, before studying slip flows over surface-attached bubble, the effectiveness of the method to trap the gas bubble by the wettability step should be verified. Inspired by the experimental method for measuring the contact angle on a solid surface, we carried out MD simulations of a nanodroplet on a chemically patterned substrate. The MD parameter values used in the setup for the contact line pinning are the same as in simulations described in Section 3.2. In general, the wetting properties of a surface are determined by the contact angle, $\theta = cos^{-1}[(\gamma_{gs} - \gamma_{sl})/\gamma]$, where γ_{gs}, γ_{sl}, and γ refer to the solid–gas, solid–liquid and liquid–gas interfacial tensions, respectively. By definition, the contact angle of a liquid droplet on a non-wetting surface is larger than on a wetting surface. In the case of chemically heterogeneous surfaces, a liquid droplet can be pinned by a wettability step, as shown schematically in Fig. 2(a). Consequently, such systems will exhibit the contact angle hysteresis $\Delta\theta$, which is defined as $\Delta\theta = \theta_2 - \theta_1$, where θ_1 and θ_2 are the contact angles on wetting and non-wetting surfaces, respectively. Therefore, the three-phase contact line of the gas–liquid interface can be pinned by the capillary force $F_{max} = \gamma c(cos\theta_2 - cos\theta_1)$, where c is the length of the contact line (Furmidge, 1962).

To examine the pinning mechanism of the three-phase contact line, we carried out a set of separate MD simulations of a liquid droplet slowly growing on the heterogeneous substrate, as shown in Fig. 2(b). In this setup, the stationary (non-wetting) upper wall was patterned by a circular wetting region with radius of 15 Å. A pore with radius of 7.5 Å was created in the center of the wetting region to allow the liquid flow from the liquid domain confined by two walls. The lower wall was set to move upward with a constant velocity U_y= 60 Å/ns, which is slow enough to permit a quasi-static growth of the droplet interface [see Fig. 2(b)]. The shape of the liquid–gas interface was determined by fitting a circle around the outermost liquid atoms. Then, the contact angle θ was measured at the intersection of the solid surface and liquid–gas interface. Fig. 2(c) shows the dependence of the contact angle θ as a function of time. The time evolution of the droplet interface involves the linear regime of pinned contact line followed by the regime when the contact line slides. During the first regime (within about 0.5ns), the contact line is pinned by the wettability step, and the contact angle gradually increases due to liquid injection. In the second regime, the contact line becomes de-pinned and starts sliding along the surface [shown in Fig. 2(d)], and, as a result, the contact angle remains nearly constant. In what follows, we define the critical contact angle θ_2 when the contact line is de-pinned.

Fig. 3 shows the variation of the critical contact angle as a function of the solid–liquid interaction energy of the non-wetting region, while the surface energy of the wetting region is fixed (ε_{sl}= 0.043*eV*). To reduce sampling errors, the contact angles were measured at five consecutive times (t_0, t_0 + 0.1, t_0 + 0.2, t_0 + 0.3 and t_0 + 0.4ns), where t_0 represents the initial time when the contact

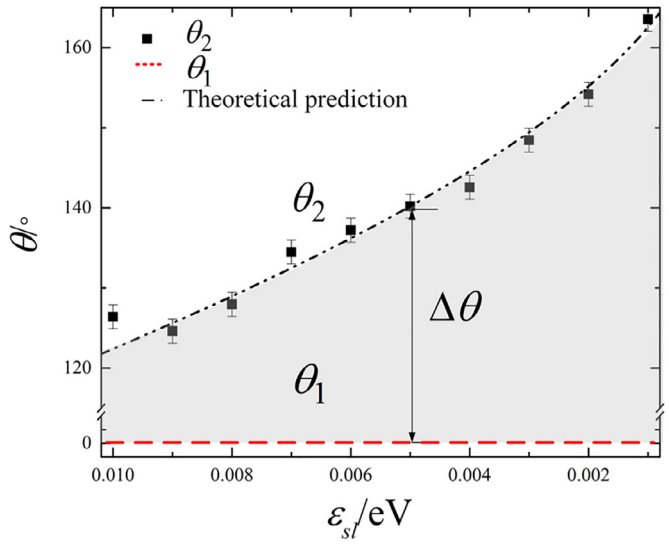

Fig. 3. The critical contact angles as a function of the surface energy of non-wetting regions. Here, θ_2 is the critical contact angle in the de-pinned state (see text for details), θ_1 is the contact angle for the wetting region, and $\Delta\theta$ is the contact angle hysteresis due to wettability step.

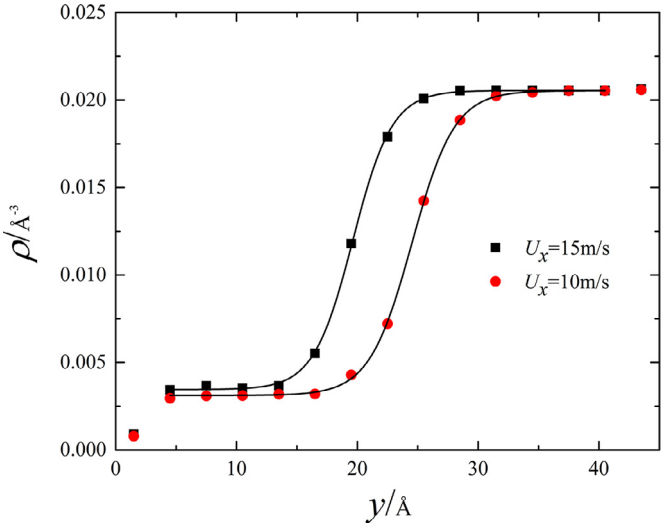

Fig. 4. The averaged density profiles across the gas–liquid interface computed at ($x = 100.5$ Å, $z = 49.5$ Å) for the indicated upper wall speeds. Symbols (■, •) represent atomic densities for $U_x = 15m/s$ and $U_x = 10m/s$. The solid curves (—) show the best fit of the data using $\rho = a - b \times tanh(2 \times \frac{y-c}{d})$ (Furmidge, 1962).

line is de-pinned. The average value of the angle obtained from these measurements was chosen as the critical contact angle θ_2. The solid symbols in Fig. 3 indicate the average values of the critical contact angle θ_2. The error bars denote the standard deviation of 5 sets of image data calculation. The black double-dotted curve and the red dashed line are the theoretical predictions for θ_2 and θ_1 from $\theta = cos^{-1}[2\varepsilon_{sl}/\varepsilon - 1]$. It can be seen from Fig. 3 that numerical values of the contact angle agree well with the theoretical prediction. The gray area in Fig. 3 shows the range of contact angles with the pinned contact line depending of the volume of liquid droplet.

3.2. The local and effective slip flows over the gas–liquid interface

We begin our analysis of shear flow over a smooth substrate with the attached nanobubble by examining the local fluid density profiles. The number of gas atoms that form a nanobubble is kept the same (unless specified otherwise) for different flow conditions. As discussed in Section 2, the computational domain was divided into small averaging bins, and, in steady state, the gas and liquid atoms were counted separately in each bin. Then, the local density profiles were obtained by combining the densities of liquid and gas phases. Fig. 4 shows the averaged density profiles across the gas–liquid interface computed at the center of the non-wetting region ($x = 100.5$Å, $z = 49.5$ Å) for the indicated upper wall speeds. The location of the gas–liquid interface is defined by the position of the density profile at $\rho = 0.5 \times (\rho_l + \rho_g)$, (Yong and Zhang, 2013b),where ρ_l and ρ_g are the average densities under different shear. As shown in Fig. 4, the liquid density away from the wall is nearly constant. Note that the gas density is slightly larger at higher shear due to compressibility of the gas phase under flow (see also the supplementary information section). A similar effect was reported in the previous MD study (Yong and Zhang, 2013a). We also find that the bubble is deformed under shear flow, and, thus, its thickness in the center of the non-wetting region ($x = 100.5$ Å, $z = 49.5$ Å) becomes smaller with increasing U_x (see Fig. 4).

Furthermore, Fig. 5(a)–(c) shows the shape of the gas–liquid interface and slip velocity distribution for different upper wall speeds ($U_x = 5$ m/s, 10 m/s, 20 m/s). The location of the gas–liquid interface was defined from the density profiles (as discussed above) and only fluid atoms in each bin were counted to compute the slip velocity, u_{gli}, at the gas–liquid interface. As illustrated in Fig. 5(a)–(c), the shape of the bubble is significantly deformed at larger upper wall speeds due to higher viscous stress. Its advancing contact angle increases and, correspondingly, the receding contact angle decreases. The final shape of the interface in steady state is determined by the competition between the capillary and viscous forces. When the advancing contact angle increases up to the value of the contact angle at the wetting surface (θ_1), and/or the receding contact angle decreases to the contact angle at the non-wetting surface (θ_2), the capillary force increases up to the maximum value and the deformation of the bubble surface reaches a critical state.

In our simulations, the three-dimensional static grid was used to compute the time-averaged density $[\rho(x,y,z)]$ and velocity $[u_x(x,y,z)]$ fields. In what follows, we consider the local velocity profiles $u_x(y)$ along the y direction at specified locations along the xz plane (see Fig. 1). This method of computing velocity profiles is different from the one used in the previous MD studies (Lee et al., 2008; Nizkaya et al., 2016; Hemeda et al., 2016), where velocity profiles (normal to the walls) were averaged over the whole area of a liquid–solid interface. We emphasize that the local velocity profiles defined in the present study allow us to investigate the local slip variation at different locations of the gas–liquid interface. For example, Fig. 5(d) shows the representative velocity profiles perpendicular to the walls at three indicated locations [marked in Fig. 5(b)]. At the location 1 (the highest location on the gas–liquid interface), the fluid velocity profile varies from $y = 25.5$ Å to $y = 100$ Å at the center of the non-wetting region ($x = 100.5$ Å and $z = 49.5$ Å). It can be seen from Fig. 5(d) that the velocity profile at the location 1 consists of two linear parts: the first part is far from the gas–liquid interface and the second part is near the gas–liquid interface. The slope of the first linear part of the velocity profile is larger than the slope of the second linear segment. These features of the velocity profile have also been observed in the previous experimental study (Schaffel et al., 2016). In the case of location 2, which is closer to the lower wall than location 1, the slope of the velocity profile is not changed significantly across the fluid domain. At the location 3, the linear velocity profile extends across the whole channel except near the walls. The slight curvature in the velocity profile, show in Fig. 5d [case 3], implies

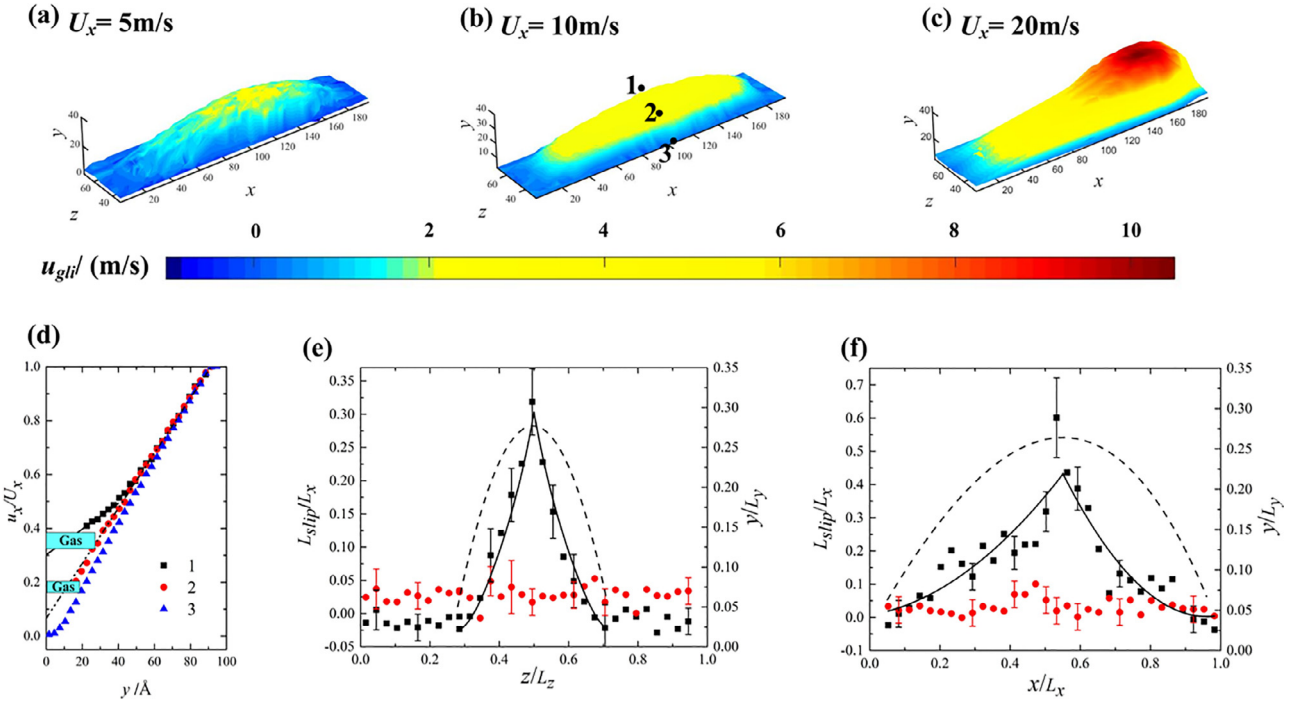

Fig. 5. The slip velocities and slip lengths for a composite interface with the surface-attached nanobubble. The dimensions of the non-wetting region are $L \times W = 190$ Å $\times$ 40 Å, the contact angle is $\theta_2 = 160^{\circ}$, U_x is the upper wall speed, and u_{gli} is the averaged velocity in small bins near the gas–liquid interface. (a), (b), (c) are the location of the gas–liquid interfaces determined from the density profiles and slip velocity distribution when U_x is 5 m/s, 10 m/s, 20 m/s. (d) is the fluid velocity profiles $u_x(y)$ plotted from the location of gas–liquid interface to the upper wall, and the observation point coordinates here are 1(100.5 Å, 25.5 Å, 49.5 Å), 2(100.5 Å, 15.5 Å, 40.5 Å), 3(100.5 Å, 0 Å, 28.5 Å), respectively. Panels (e) and (f) show the local and effective slip lengths at $x = 100$ Å in the zy plane and at $z = 50$ Å in the xy plane for $U_x = 10m/s$. Symbols and lines (- - -, ■, —, •) indicate the gas–liquid interfaces on the right-*vertical* axis, the local slip length on the left-*vertical* axis, fit of the local slip length, and the effective slip length on the left-*vertical* axis, respectively. The typical error bars are based on three independent runs.

a negative value of the local slip length and enhanced viscosity of the adjacent layers.

Given these distinct features of the velocity profiles, we examined two kinds of slip lengths; namely, the *effective slip length* (L_{eff}) and *local slip length* (L_{local}). Both slip lengths were calculated using the Navier's slip model, $v_{slip}=L_{slip}(du_x/dy)$, where v_{slip} is the slip velocity obtained by extrapolating a linear part of the velocity profile to the position ($y = 0$). The *effective slip length* is extracted by fitting a linear function to the velocity profile in the central flow region [dashed line in Fig. 5(d)], while the *local slip length* is calculated by fitting a linear function (Furmidge,1962) to the velocity profile near the interface [solid line in Fig. 5(d)]. Thus, the difference between L_{eff} and L_{local} originates from different slopes of the velocity profiles used to fit the MD data. In our analysis, we used at least four data points near the gas–liquid interface to calculate the *local slip length* and ten data points near the upper wall to determine the *effective slip length*. Note that the velocity profiles near the solid surface are influenced by the solid atoms, leading to a slight curvature in the velocity profile near the walls (Priezjev and Troian, 2004). This curvature introduces a small error in an estimate of the *local slip length*. In our study, we discarded the first data points near the solid walls to calculate the *local slip length* at the wetting region without the gas–liquid interface.

In order to provide further insight on the slip behavior at the gas–liquid interface, the distribution of the local and effective slip lengths is presented in Fig. 5(e) and (f) that were computed at $z = 50$ Å in the xy plane and at $x = 100$ Å in the zy plane, respectively. Our numerical results demonstrate that L_{eff} is nearly constant along the gas–liquid interface. This is expected since the effective slip length describes the flow far away from the interface, and, hence, the distribution of the effective slip length is not significantly influenced by the composite interface. By contrast, L_{local} strongly depends on the location along the gas–liquid interface. Along the zy plane, which is oriented perpendicular to the flow direction, the local slip lengths are symmetric with respect to the center of the non-wetting region due to symmetry of the flow. However, in the plane of shear, L_{local} becomes asymmetric which is caused by the deformation of the bubble surface in the flow.

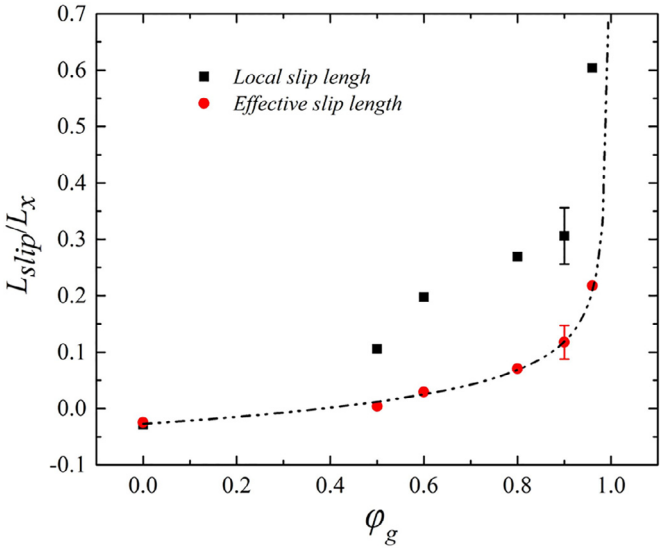

Fig. 6. The local and effective slip lengths as a function of the gas areal fraction. The upper wall velocity is $U_x = 10m/s$. The dash-dotted curve is the best fit of the MD data to Eq.(4). The error bars show variation of the data from three independent samples.

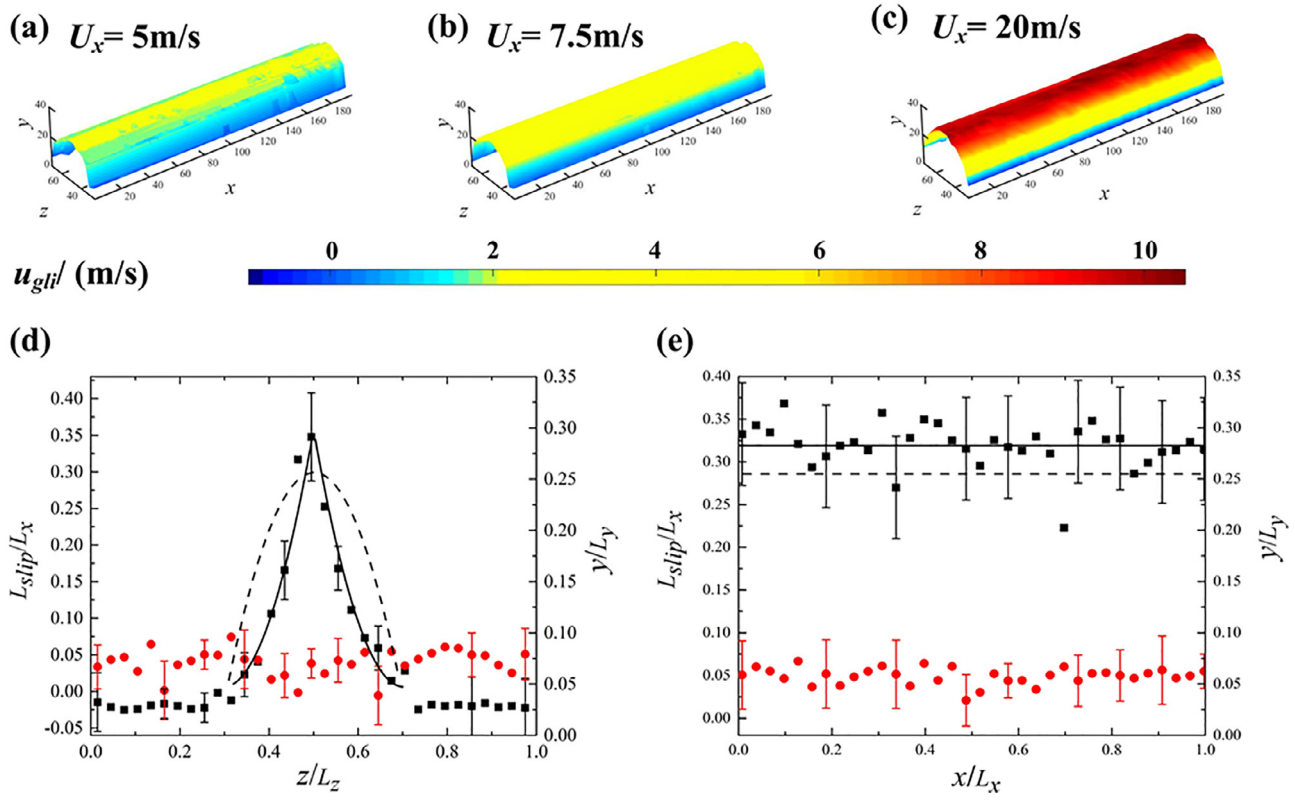

Fig. 7. The spatial distribution of slip velocity and slip lengths for a continuous gas–liquid interface. The area of non-wetting region is $L \times W = 200$ Å $\times$ 40 Å and the wettability contrast is $\theta_2 - \theta_1 = 160^\circ$. Shown in (a), (b), (c) are the gas–liquid interfaces and slip velocity distribution when U_x is 5 m/s, 7.5 m/s, 20 m/s. Panels (d) and (e) show the local and effective slip lengths at $x = 100$ Å in the zy plane and at $z = 50$ Å in the xy plane for $U_x = 10m/s$. Symbols and lines (– –, ■, —, •) denote the gas–liquid interfaces on the right-*vertical* axis, the local slip length on the left-*vertical* axis, fit of the local slip length and the effective slip length on the left-*vertical* axis, respectively.

Next, we investigate the influence of the area covered by the bubble, $\varphi_g = LW/L_xL_z$, on slip lengths. The gas areal fraction was varied by changing the length of the non-wetting region, while its width was kept fixed to W = 96 Å. Due to the finite thickness of a surface-attached bubble, the interface curvature near the contact line is non-zero. In order to make the interface smoother and to facilitate the comparison of the simulation results with the theoretical prediction of Eq. (2) below, we adjusted the number of gas atoms to keep the height of the bubble to be about 8 Å at different gas areal fractions. The variation of the number of gas atoms slightly affects the density of the gas phase and introduces the maximum error of 0.3 Å in an estimate of the location of the gas–liquid interface. Our MD results for the slip lengths as a function of the gas areal fraction are summarized in Fig. 6, where the effective and local slip lengths were calculated in the center of the non-wetting region ($x = 100.5$ Å, $z = 49.5$ Å).

Generally, the flow over a surface with a smooth liquid–gas interface trapped by holes is described by the effective slip length, which scales with the gas areal fraction as follows (Lauga and Stone, 2003)

$$L_{eff} \sim -\ln(1 - \varphi_g). \tag{2}$$

In addition, a finite contribution to the effective slip length might arise from the intrinsic slip, which represents the slip length caused by liquid–solid contact. It is calculated by fitting the central flow region on a smooth solid surface, which is defined as the wetting region in our study. It has been suggested that the extra slip induced by the intrinsic slip length L_s^i of the liquid–solid scales with φ_g has the following contribution (Lauga and Stone, 2003):

$$L_{eff} \sim L_s^i/(1 - \varphi_g). \tag{3}$$

In our MD setup, the intrinsic slip length is measured $L_s^i = -0.015L_x$ for the uniformly wetting region with the wall-fluid interaction energy $\varepsilon_{sl} = 0.043eV$. The negative value of the slip length is typically obtained when the surface energy "ε_{sl}" is large and the first few layers of fluid near the wall become locked to the surface and thus can be regarded as epitaxial layers (Thompson and Robbins, 1990; Lichter et al., 2007). In this case, the slip length is negative as it was calculated by extrapolating the parabolic fit of velocity profile with respect to the wall-fluid interface. Higher degree of locking of fluid layers leads to more negative values of the slip length.

As is evident from Fig. 6, the simulation results for the effective slip length can be accurately described by the following function

$$L_{eff}/L_x = -[0.05255ln(1 - \varphi_g) + 0.0297] - 1.8 \times L_s^i/[L_x(1 - \varphi_g)]. \tag{4}$$

The fitting coefficients of Eq. (4) are numerical prefactors, which are expected to depend on the underlying geometry of the surface (stripes, posts, etc.) (Ybert et al., 2007). By qualitative comparisons between our work and previous studies (Ybert et al., 2007; Ng and Wang, 2010; Yong and Zhang, 2013b), we found: For $0 \le \varphi_g \le 1$, the intercept of our fitting results agrees with the semianalytical solution $L_{eff} = -L_x[0.134ln(1 - \varphi_g) + 0.023]$ (Ng and Wang, 2010), and the slope also shows a reasonable agreement. However, the fitting coefficients of the intrinsic slip length are different from the results by Yong and Zhang (2013b), due to the positive value of the intrinsic slip length on the solid wall used in that study.

In comparison with the results of the recent MD study (Tretyakov and Muller, 2013) on the behavior of the effective slip over grooved superhydrophobic surfaces, the friction induced by the groove edges facing the flow need not be accounted for in

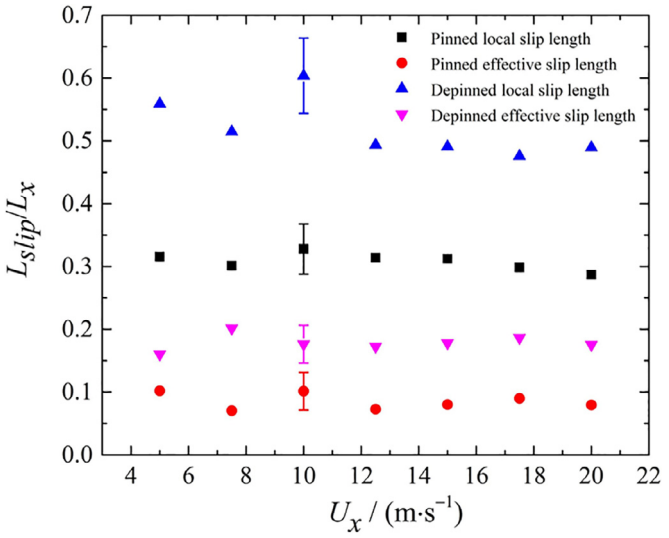

Fig. 8. The local and effective slip lengths at the gas–liquid interface in the center of the non-wetting region ($x = 100.5$ Å, $z = 49.5$ Å) as a function of the upper wall speed. The areas of the non-wetting regions are $L \times W = 190$ Å $\times$ 90 Å and $L \times W = 200$ Å $\times$ 90 Å for pinned and continuous gas–liquid interfaces, respectively. The wettability step is $\theta_2 - \theta_1 = 160^{\circ}$. The typical error bars are based on three independent runs.

our study, because the nanobubble is trapped on a smooth surface without topographical surface roughness.

As seen in Fig. 6, the local slip length L_{local} is nearly equal to L_{eff} for uniformly wetting interface. In the presence of the liquid–gas interface, both L_{local} and L_{eff} increase with φ_g but L_{local} is always larger than L_{eff} at a given gas areal fraction. As the gas areal fraction increases from 0.9 to 1.0, the gas–liquid interface becomes continuous along the flow direction, and the effective slip length increases from $0.1L_x$ to $0.3L_x$, while the local slip length increases from $0.3L_x$ to $0.6L_x$. These results indicate that the interface continuity (pinned or continuous) can significantly influence the local and effective slip lengths. To clarify this issue, below we present a detailed analysis of the slip length distribution in the case of a continuous gas–liquid interface when the contact line perpendicular to the shear flow direction is absent.

The contour plots of the liquid–solid interfaces and slip velocities in the shear flow direction as well as the corresponding slip lengths are reported in Fig. 7 for the selected upper wall speeds. As shown in Fig. 7 (a)–(c), the shape of the continuous gas–liquid interface is markedly different from the shape of the pinned bubble considered in Fig. 5. To remind, in the pinned case, the effective surface roughness in the flow direction was introduced by the curvature of the bubble surface. In contrast, the interface curvature in the flow direction is absent for the continuous gas–liquid interface, and, hence, the flow streamlines are straight. Therefore, the continuous interface remains almost undeformed even at the largest upper wall speed, $U_x = 20 m/s$, considered in the present study.

Next, the local and effective slip length distribution at $z = 50$ Å in xy plane and $x = 100$ Å in the zy plane are plotted in Fig. 7(d) and (e). Similar to the pinned gas–liquid interface, L_{eff} remains nearly constant along the continuous interface, but its magnitude is twice as large. Along the zy plane, the distribution of the local slip lengths is similar to the pinned case. However, in the xy plane, the L_{local} is almost constant along the bubble surface, because the interface is straight and continuous.

Finally, we consider the influence of the upper wall speed on the local and effective slip lengths for pinned and continuous gas–liquid interfaces. As shown in Fig. 8, the effective and local slip lengths remain nearly constant with increasing shear rate for both types of interfaces. Although the deformation of the pinned interface is considerable at the largest upper wall speed $U_x = 20$ m/s, the change of the slip length is not significant. Thus, the local slip behavior at the nanoscale is drastically different from the previous results at the microscale which showed that, with increasing shear rate, the slip length is gradually reduced due to deformation of bubbles (Lee et al., 2008; Teo et al., 2014). On the other hand, the simulation results presented in Fig. 8 agree well with the results of the study by Yong and Zhang on the slip behavior at interfaces that contain bubbles trapped at a hole (Yong and Zhang, 2013b), where no significant dependence of the slip length on shear rate was found. It can also be observed in Fig. 8 that the local and effective slip lengths for flow over continuous interfaces are much greater than in the case of a pinned nanobubble for a given value of the upper wall speed. These results suggest that slip flow over continuous gas–liquid interfaces, rather than pinned interfaces, might lead to significant drag reduction. This might also be one of the contributing factors explaining the deviation between experimental measurements of drag reduction by non-wetting surfaces and the theoretical prediction of de Gennes (2002). Typically, the non-wetting surfaces used in experiments trap the gas–liquid interface by micro- or nano-scale holes, whose edges pin the contact line of the gas–liquid interfaces. However, in the de Gennes' argument, a continuous gas–liquid interface on a smooth surface was assumed. Thus, one can expect that a continuous gas–liquid interface is more advantageous for applications that involve drag reduction.

4. Conclusions

In this paper, we investigated the behavior of the local and effective slip lengths that describe shear flows over nanobubbles attached to smooth solid surfaces using molecular dynamics simulations. We considered atomically flat surfaces with regions of mixed wettability that effectively trap gaseous nanobubles, which remain stable even at high shear rates. Our main results can be summarized as follows. First, we demonstrated that the contact line at the gas–liquid interface can be pinned by the wettability step on atomically smooth substrate and the contact angle hysteresis depends strongly on the wettability contrast. Second, the local slip length L_{local} is finite at the gas–liquid interface and its spatial distribution becomes asymmetric due to deformation of the nanobubble under high shear. In contrast, the effective slip length L_{eff} is nearly constant along the gas–liquid interface as it describes the flow far away from the composite interface. Last, both local and effective slip lengths are larger for continuous gas–liquid interfaces where the effective surface roughness due to the interface curvature in the flow direction is absent. In other words, a significant drag reduction can be achieved for flows over smooth surfaces with continuous stripe-like gas–liquid interfaces rather than over a sequence of isolated nanobubbles. It can be inferred from our results that the gas–liquid interface will promote the effective slip and result in apparent drag reduction. Meanwhile, the liquid flow near the gas–liquid interface is more sensitive to the local boundary conditions than the flow in the region far away from the interface. It is also shown that different regions of the gas–liquid interface are characterized by their own local slip lengths, however, the effective slip length is obtained from the integration of the local slip length over the whole domain. Apart from the global flow behavior, the correct modeling of the local flows relies on the correct assumption for the local slip boundary conditions at gas–liquid interfaces and near the contact line. Further investigations are still needed to establish the quantitative relation between the local and effective slip lengths.

Acknowledgments

This work was supported by the National Natural Science Foundation of China (Grant No. 51679203), the Natural Science Basic Research Plan in Shaanxi Province of China (Grant No. 2016JM1002), and the Natural Science Basic Research Plan in Shenzhen city of China (Grant No. JCYJ20160510140747996). The third author also acknowledges financial supports from the Innovation Foundation for Doctoral Dissertation (Grant No. CX201501) and the Excellent Doctorate Foundation of Northwestern Polytechnical University.

Supplementary materials

Supplementary material associated with this article can be found, in the online version, at doi:10.1016/j.ijmultiphaseflow.2018.03.001.

References

Bidkar, R.A., Leblanc, L., Kulkarni, A.J., Bahadur, V., Ceccio, S.L., Perlin, M., 2014. Skin-friction drag reduction in the turbulent regime using random-textured hydrophobic surfaces. Phys. Fluids 26, 263–290.
Bolognesi, G., Cottin-Bizonne, C., Pirat, C., 2014. Evidence of slippage breakdown for a superhydrophobic microchannel. Phys. Fluids 26, 082004.
Choi, C.H., Ulmanella, U., Kim, J., Ho, C.M., Kim, C.J., 2006. Effective slip and friction reduction in nanograted superhydrophobic microchannels. Phys. Fluids 18, 087105.
Cottin-Bizonne, C., Barentin, C., Bocquet, L., 2012. Scaling laws for slippage on superhydrophobic fractal surfaces. Phys. Fluids 24, 012001.
de Gennes, P.G., 2002. On fluid/wall slippage. Langmuir 18, 3413–3414.
Feng, J.Q., Basaran, O.A., 1994. Shear-flow over a translationally symmetrical cylindrical bubble pinned on a slot in a plane wall. J. Fluid Mech. 275, 351–378.
Furmidge, C.G., 1962. Studies at phase interfaces .1. sliding of liquid drops on solid surfaces and a theory for spray retention. J. Colloid Sci. 17, 309.
Hemeda, A.A., Tafreshi, H.V., 2016. Liquid-infused surfaces with trapped air (LISTA) for drag force reduction. Langmuir 32, 2955–2962.
Hyvaluoma, J., Kunert, C., Harting, J., 2011. Simulations of slip flow on nanobubble-laden surfaces. J. Phys.Condes. Matter 23, 184106.
Karatay, E., Haase, A.S., Visser, C.W., Sun, C., Lohse, D., Tsai, P.A., Lammertink, R.G.H., 2013. Control of slippage with tunable bubble mattresses. Proc. Natl. Acad. Sci. USA 110, 8422–8426.
Lauga, E., Stone, H.A., 2003. Effective slip in pressure-driven Stokes flow. J. Fluid Mech. 489, 55–77.
Lee, C., Choi, C.H., Kim, C.J., 2008. Structured surfaces for a giant liquid slip. Phys. Rev. Lett. 101, 064501.
Lee, C., Kim, C.J., 2009. Maximizing the giant liquid slip on superhydrophobic microstructures by nanostructuring their sidewalls. Langmuir 25, 12812–12818.
Lichter, S., Martini, A., Snurr, R.Q., Wang, Q., 2007. Liquid slip in nanoscale channels as a rate process. Phys. Rev. Lett. 98, 226001.
Maali, A., Boisgard, R., Chraibi, H., Zhang, Z., Kellay, H., Wurger, A., 2017. Viscoelastic drag forces and crossover from no-slip to slip boundary conditions for flow near air-water interfaces. Phys. Rev. Lett. 118, 084501.
Ng, C.O., Wang, C.Y., 2010. Apparent slip arising from Stokes shear flow over a bidimensional patterned surface. Microfluid. Nanofluid. 8, 361–371.
Nizkaya, T.V., Dubov, A.L., Mourran, A., Vinogradova, O.I., 2016. Probing effective slippage on superhydrophobic stripes by atomic force microscopy. Soft Matter 12, 6910–6917.
Ou, J., Perot, B., Rothstein, J.P., 2004. Laminar drag reduction in microchannels using ultrahydrophobic surfaces. Phys. Fluids 16, 4635–4643.
Ou, J., Rothstein, J.P., 2005. Direct velocity measurements of the flow past drag-reducing ultrahydrophobic surfaces. Phys. Fluids 17, 103606.
Plimpton, S., 1995. Fast parallel algorithms for short-range molecular-dynamics. J. Comput. Phys. 117, 1–19.
Priezjev, N.V., Troian, S.M., 2006. Influence of periodic wall roughness on the slip behaviour at liquid/solid interfaces: molecular scale simulations versus continuum predictions. J. Fluid Mech. 554, 25.
Priezjev, N.V., Troian, S.M., 2004. Molecular origin and dynamic behavior of slip in sheared polymer films. Phys. Rev. Lett. 92, 018302.
Qian, T.Z., Wang, X.P., Sheng, P., 2003. Molecular scale contact line hydrodynamics of immiscible flows. Phys. Rev. E 68, 016306.
Razavi, S., Koplik, J., Kretzschmar, I., 2014. Molecular dynamics simulations: insight into molecular phenomena at interfaces. Langmuir 30, 11272–11283.
Rothstein, J.P., 2010. Slip on superhydrophobic surfaces. Annu. Rev. Fluid Mech. 42, 89–109.
Schaffel, D., Koynov, K., Vollmer, D., Butt, H.J., Schonecker, C., 2016. Local flow field and slip length of superhydrophobic surfaces. Phys. Rev. Lett. 116, 134501.
Teo, C.J., Khoo, B.C., 2014. Effects of interface curvature on Poiseuille flow through microchannels and microtubes containing superhydrophobic surfaces with transverse grooves and ribs. Microfluid. Nanofluid. 17, 891–905.
Thompson, P.A., Robbins, M.O., 1990. Origin of stick-slip motion in boundary lubrication. Science 250, 792–794.
Tretyakov, N., Muller, M., 2013. Correlation between surface topography and slippage: a molecular dynamics study. Soft Matter 9, 3613–3623.
Thalakkottor, J.J., Mohseni, K., 2016. Unified slip boundary condition for fluid flows. Phys. Rev. E 94, 023113.
van Limbeek, M.A.J., Seddon, J.R.T., 2011. Surface nanobubbles as a function of gas type. Langmuir 27, 8694–8699.
Vinogradova, O.I., Belyaev, A.V., 2011. Wetting, roughness and flow boundary conditions. J. Phys.Condes. Matter 23, 184104.
Yang, S.J., Dammer, S.M., Bremond, N., Zandvliet, H.J.W., Kooij, E.S., Lohse, D., 2007. Characterization of nanobubbles on hydrophobic surfaces in water. Langmuir 23, 7072–7077.
Ybert, C., Barentin, C., Cottin-Bizonne, C., Joseph, P., Bocquet, L., 2007. Achieving large slip with superhydrophobic surfaces: scaling laws for generic geometries. Phys. Fluids 19, 123601.
Yen, T.H., 2015. Effects of wettability and interfacial nanobubbles on flow through structured nanochannels: an investigation of molecular dynamics. Mol. Phys. 113, 3783–3795.
Yong, X., Zhang, L.T., 2013a. Thermostats and thermostat strategies for molecular dynamics simulations of nanofluidics. J. Chem. Phys. 138, 084503.
Yong, X., Zhang, L.T., 2013b. Toward generating low-friction nanoengineered surfaces with liquid-vapor interfaces. Langmuir 29, 12623–12627.